의학박사 학위논문

Development of an Automated Diagnosis System of Optic Neuropathy in Digital Fundus Photographs

디지털 안저사진에서 시신경병증
자동진단장비 개발

2018년 8월

서울대학교 대학원

의학과 안과학전공

양 희 경

Abstract

Development of an Automated Diagnosis System of Optic Neuropathy in Digital Fundus Photographs

Hee Kyung Yang

Ophthalmology Major

Graduate School of Medicine

Seoul National University

Assessment of the morphological characteristics of the optic nerve on digital fundus photographs is a critical step in making the correct diagnosis in optic neuropathy. However, optic disc morphology on fundus photographs can exhibit similar findings in various diseases, which makes it hard to distinguish between different etiologies solely based on morphological assessment. Despite the extensive use of quantitative imaging techniques such as optical coherence tomography (OCT) nowadays, most of the health care centers and primary eye care clinics use digital fundus photography as an initial screening tool for posterior segment eye diseases due to its cost−effective and feasible

nature. The interpretation of digital fundus photographs in the common clinical setting rely on manual detection by an examiner, which is subject to interindividual variability. Thus, to improve the accuracy of interpretation of fundus photographs, we developed a fully automated novel computer-aided detection (CAD) system for optic disc morphology on fundus photographs. The performance of the system in differentiating subjects with normal optic discs and those with RNFL defects and optic disc pallor showed an accuracy of 94% and 96%, respectively. The efficacy of the CAD system in diagnosing optic neuropathy during mass screening of fundus photographs in a single health care center was 90%.

....

Table of Contents

List of Tables

List of Figures

Chapter 1. Introduction

Assessment of the morphological characteristics of the optic nerve on digital fundus photographs, including optic disc pallor, notching, cupping and retinal nerve fiber layer (RNFL) defects together with the associated retinal findings is a critical step in making the correct diagnosis in patients with optic neuropathy. However, optic disc morphology on fundus photographs can exhibit similar findings in various diseases, which makes it hard to distinguish between different etiologies solely based on morphological assessment. Despite the extensive use of quantitative imaging techniques such as optical coherence tomography (OCT) nowadays, most of the health care centers and primary eye care clinics use digital fundus photography as an initial screening tool for posterior segment eye diseases due to its cost-effective and feasible nature. The interpretation of digital fundus photographs in the common clinical setting rely on manual detection by an examiner, which is subject to interindividual variability. Thus, to improve the accuracy of interpretation of fundus photographs, we developed a fully automated novel computer-aided detection (CAD) system for optic disc pallor on fundus photographs, and validated its performance in detecting optic neuropathy among normal fundus photographs and

during mass screening in a large population who visited a single healthcare center.

Chapter 2. Automatic Computer−Aided Diagnosis of Retinal Nerve Fiber Layer Defects in Fundus Photographs

2.1. INTRODUCTION

Retinal nerve fiber layer (RNFL) defects such as localized thinning or loss of the RNFL, including papillomacular bundle defects,[1, 2] is a major sign that precedes detectable optic disc changes and visual field loss in the early stages of glaucoma or other non− glaucomatous optic neuropathies.[3, 4] Glaucoma leads to structural changes of the optic disc and RNFL and advanced visual field loss. Because such changes are generally irreversible, early diagnosis and treatment are critical.[5, 6] Papillomacular bundle defect is also a major sign of various hereditary, toxic, and mitochondrial optic neuropathies, and early detection of such changes can facilitate the clinical diagnosis and decision−making. [3, 4]

Various methods are available for examining RNFL defects. Heidelberg retina topography (HRT), scanning laser polarimetry (SLP), and optical coherence tomography (OCT) can accurately produce quantitative measurements of the optic disc and RNFL.[5]

However, these technologies are expensive and require a trained technician.[7] Fundus photography is the most commonly used and cost−effective imaging tool that can be performed as part of the routine medical check−up; thus, it has an enormous potential for community glaucoma screening in remote or non−hospital environments.[8] However, RNFL defects are thin and shallow in the early stages of glaucoma, which makes them difficult to detect. Fundus photographs may have sharper boundaries for RNFL defects showing early defects on fundus photographs, while OCT results may not be definitely decreased in thickness compared to the age− matched normal population, with only a relative thinning compared to other sectors observed. Further, the detection rates are highly dependent on the experience of the examiner. Therefore, the development of a method that is more sensitive and reliable for detecting RNFL defects on fundus photographs for use as a diagnostic tool for glaucoma and various optic neuropathies is important.

In this work, we have proposed a simple and efficient algorithm for the automatic detection of RNFL defects that can alert ophthalmologists to the location of possible RNFL defects. We tested its validity in patients with localized RNFL defects with glaucoma and other hereditary and toxic optic neuropathies.

2.2. METHODS

Subjects and Fundus Photographs

This study included the fundus photographs of 98 subjects with 140 localized RNFL defects and 100 fundus photographs of healthy normal subjects who did not have any history of ocular diseases and had normal RNFL and optic disc appearance on fundus photographs. The subjects consisted of 89 patients with early to moderate glaucoma, and their mean deviation was −4.06 ± 3.44 dB (range, −12.87 ~ −0.03) by the Humphrey Field Analyzer, and 9 patients with non−glaucomatous optic neuropathy with papillomacular bundle defects: 4 patients with Leber's hereditary optic neuropathy, 3 patients with autosomal dominant optic atrophy, and 2 patients with toxic optic neuropathy.

The fundus images were obtained from Seoul National University Bundang Hospital. All images were photographed by using the digital Nikon D80 camera (Nikon Co. Ltd. Tokyo, Japan) equipped with a KOWA VX−10 fundus camera (Kowa Company Ltd., Tokyo, Japan), and were taken as 24−bit color images. Images of various sizes were resized to a resolution of 1278 × 848 pixels in order to reduce the computational time and to minimize the effects of small pathological regions. Two ophthalmologists independently marked

the region of the RNFL defects and when both reviewers determined the presence of RNFL defect, the case was considered to have an RNFL defect. The results of manual detection were confirmed by Stratus® OCT (Carl Zeiss Meditec, Germany) or Spectralis® OCT (Heidelberg engineering, Germany) results showing a definite or relative localized thinning of RNFL analysis compared to other sectors. The research adhered to the tenets of the Declaration of Helsinki.

Flowchart of Proposed CAD

The proposed CAD method was performed in 3 steps. First, the algorithm automatically detected the location of the main features in the fundus image, such as the optic disc, macula, and blood vessels. Then, it corrected the non-uniform illumination of the green channel image by using the bias image. Second, blood vessels were removed. Blood vessel segmentation is essential in order to achieve RNFL defect detection. Then, the image was converted to polar coordinates according to the center of the optic disc. Finally, the candidate RNFL defects were observed as vertical dark bands, and the false positives were subsequently reduced by using knowledge-based rules of the average pixel value in the candidate region, the vertical length, and the angular location. To reduce

10

perceptual errors, 2 ophthalmologists performed independent double reading of the fundus photographs. A flowchart showing the proposed CAD system for RNFL defects and the resulting images at each step is provided in Figure 2.1.
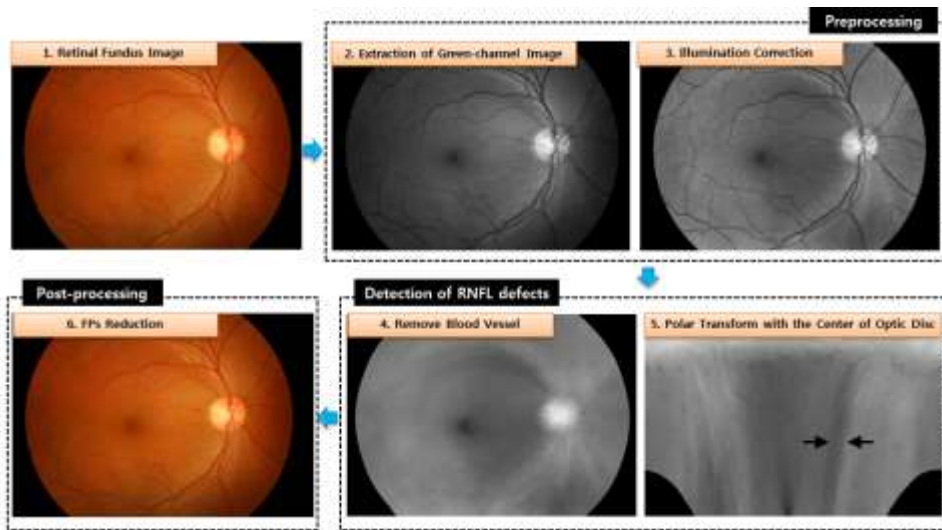
Figure 2.1 Flowchart of the proposed computer-aided diagnosis system for automatic retinal nerve fiber layer defect detection and result images at each step.

In fundus images, the RNFL defect locations were determined as clock hours, and we measured the clock-hour location of the RNFL defects in all of the cases. The clock-hour location was defined as the location from a reference line in a clockwise direction for the right eyes and in a counterclockwise direction for the left eyes

(Figure 2.2).[9] The reference line was a vertical line through the center of the circle.
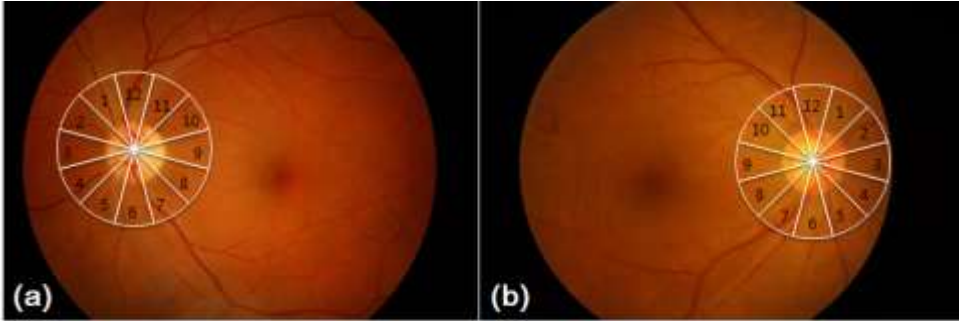
Figure 2.2 Clock-hour locations of retinal nerve fiber layer defects on fundus photographs of (a) the right eye and (b) the left eye.

Preprocessing

Preprocessing of the proposed algorithm can be divided into 2 major steps: (1) noise reduction and (2) illumination correction. We used the green channel of the color fundus image because this maximizes the contrast between the RNFL defects and blood vessels.[10]

Noise Reduction

To remove unwanted text images such as patient information, we applied a binary mask by using a morphological open operation. The binary mask extracted the region of interest (ROI) in the entire image. Then, a median filter of size 3 × 3 was applied to the

masked image to suppress noise and to maintain an edge of the image.

Illumination Correction

Non-uniform illumination by non-ideal acquisition condition and the spherical geometry of the eye can cause severe distortions in the color fundus image. This non-uniform illumination artifact is often described as 'shading' or 'bias'. Correcting the non-uniform illumination can contribute to accurate blood vessel segmentation by enhancing the contrast of the blood vessel at the periphery of the fundus image.[11-13] Zheng et al. proposed a retrospective illumination-correction method based on the sparsity of the image gradient distribution.[14] This method can automatically correct the illumination of an arbitrary fundus image by using the bias. The bias of the image denotes the spatial variations of intensity caused by illumination changes for images taken by a digital camera. The bias is a smooth field in any format, which can be represented by a bivariate polynomial, B-Spline, etc. In this study, we used the method described by Zheng et al. A given green channel image (G) assumes the product of the uniformly illuminated fundus image (I) and the bias field (B), as follows:

$$G(i, j) = B(i, j)I(i, j)$$

where (i, j) is the pixel position in the image.

An example of non-uniform illumination correction is shown in Figure 2.3. The given green channel image is shown in Figure 2.3 (a) and the bias image as the shading artifact is shown in Figure 2.3 (b). The corrected image was generated by the given green channel image divided by the bias image, as shown in Figure 2.3 (c). The intensity profiles of 1 row in the given green channel image and in the corrected image is shown in Figure 2.3 (d). This shows that the background intensity in the corrected image had greater uniformity compared to the given green image.
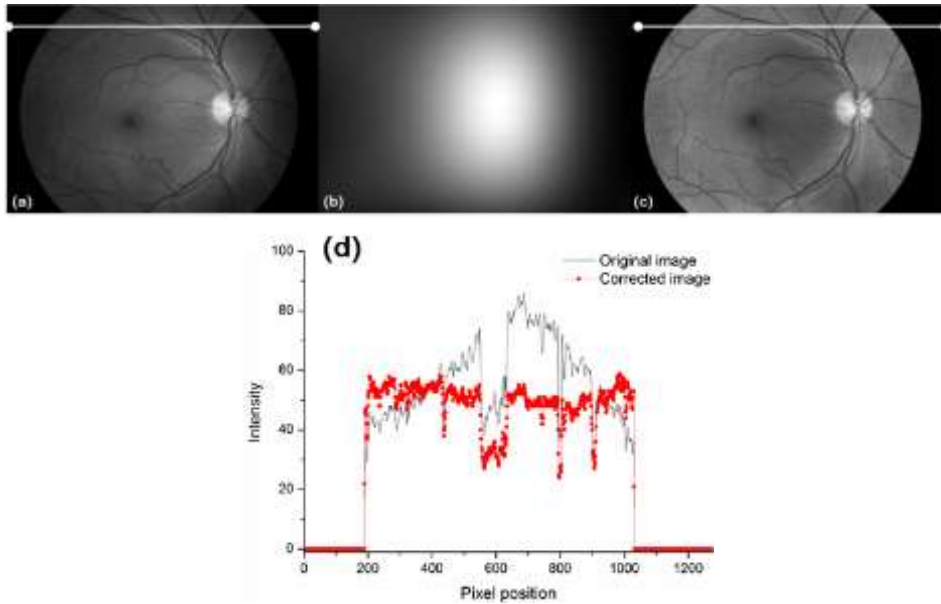
Figure 2.3 An example of non-uniform illumination correction: (a) Green channel image, (b) Estimated bias field for correction, (c) Corrected green image, (d) Intensity profiles of one row in the given green channel image and in the corrected green image.

Blood Vessel Removal

Blood vessel removal (BVR) is an essential step to detect RNFL defects more accurately. Many methods have been reported for blood vessel extraction from fundus images.[15-18] In this study, the blood vessels were extracted by using a morphological bottom-hat transform in order to detect the blood vessels as dark regions. The bottom-hat transform is defined as the difference between the closing by a disk-shaped structural element (SE) and the input

15

image. Since the maximum blood vessel width is approximately 10 pixels, the SE diameter was set to 10 pixels. Although the bottom-hat method can be used simply to detect the blood vessels, this method is not sufficient for exact extraction of the entire blood vessel structure. Therefore, we also used the Kirsch method, which is an edge detector that determines the maximum edge strength with an 8-directional filter.[15] The Kirsch method is useful for detecting the edge of large blood vessel structurea, but it is not suitable in detecting small vessels and pathological regions.

The results of blood vessel extraction after applying the bottom-hat transform, Kirsch method, and combined method are shown in Figure 2.4. To compensate for the disadvantages of the 2 methods, we combined the 2 methods for iterative use.

To reduce the false-positive (FP) rates, the pathological regions in the fundus images were detected with blood vessels, as shown in Figure 2.4. For each pixel of the segmented vessel region determined by using the combined method, the intensity value was replaced by a mean intensity that was computed over all pixels in a 61×61 neighborhood of the pixel location. The size of the neighborhood region was chosen to be a sufficiently large area to minimize the influence caused by other pathological lesions and blood vessel regions.
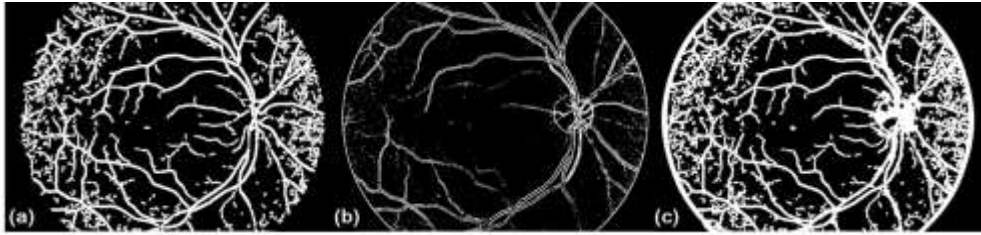
Figure 2.4 Results of blood vessel extraction from (a) bottom-hat transformation, (b) Kirsch method, and the (c) combined method.

Polar Transformation

RNFL defects appear radially from the optic disc in various forms, such as fan shaped, wedge shaped, slit-like shape, and spindle-like shape. In this study, to detect the RNFL defects effectively, the BVR image was transformed to the polar coordinates with a reference point as the location of maximum cup depth in the optic disc. Because the optic disc has high intensity in the green image, the reference point in the optic disc was detected by using a local maximum method. Further, we detected the macular center by using a local minimum method to reduce the FP rate. In the polar coordinates, a retinal location (pixel) is represented by a radial distance and angle from the reference point. Because the RNFL defects do not spread out in the radial direction completely around the optic disc, the RNFL defect lines in the polar coordinates are

slightly tilted toward the macular position. The difference of the radial widths of the defect in the polar coordinate was also negligible. Thus, we assumed that the RNFL defects in the polar coordinates were a relatively straight line in the vertical direction. The detection results of the reference point in the optic disc and the macular center are shown in Figure 2.5 (a). The polar coordinate transformation of the BVR image results is shown in Figure 2.5 (b), where the RNFL defect is marked by black arrows.
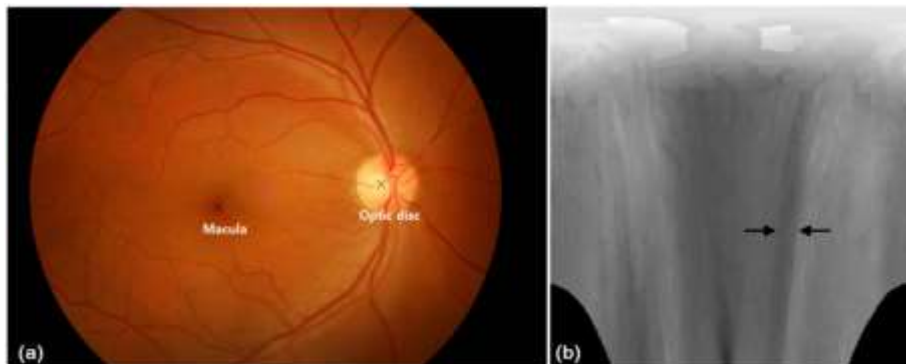
Figure 2.5 (a) Detection results for the optic disc and macular centers and (b) polar coordinate transformation of blood vessel removal image and retinal nerve fiber layer defects (black arrow). The circle region (yellow dot line) indicates the region for polar transformation and is transformed in the clockwise direction (white arrow) for the right eye from the start position.

Detection of RNFL Defects

Hough transformation was applied to detect the candidates with straight lines. The procedure for detecting RNFL defects consisted of 3 steps. First, the polar transformed image was filtered with a 2D-Gaussian filter to smooth the boundary of the blood vessel region. Then, we determined the edge of the smoothed image by using the Canny edge detection algorithm. Subsequently, the Hough transform for line detection was performed on the edge image. Finally, the candidate RNFL defects were detected, including the misdetected candidates. If the detected region of the arbitrary candidate overlapped with the region of the gold standard, it was considered a true positive (TP) detection.

False Positive Reduction

In this study, a FP represented a misdetected RNFL defect candidate. The misdetected candidates of the RNFL defects were reduced by using knowledge-based rules. For each candidate, we classified the average pixel values in the candidate region, the vertical length, and the angular location. With these 3 features, the true RNFL defects were determined. First, we extracted the average pixel values in the candidate region that were smaller compared to the average value in the surrounding background

region, except for the blood vessel region. Then, the candidates were classified by the vertical length to suppress noise. We selected the vertical lengths which were more than two times of the maximum blood vessel width in order to reduce the false detection of the blood vessel and other noise. We selected the angular location within a main vascular region (± 79° from a reference line) corresponding to the temporal sector, as this is where clinically significant loss of glaucomatous and nonglaucomatous RNFL thinning takes place. The reference line was drawn from the center of the optic disc to the macular center on the fundus image. We also excluded the macula region and the blood vessel region from the inner region of the main vascular region. The FPs were removed after FP reduction, leaving the true detected candidates.

Main Outcome Measures

The intensities and widths of the RNFL defects were measured and the detection rates according to each feature were determined for glaucoma and non−glaucomatous optic neuropathy with papillomacular bundle defects. The comparison was based on agreement in the position of the RNFL defect band and not the width.

To evaluate the performance of the proposed algorithm

quantitatively, we used free-response receiver operating characteristics (FROC) analysis.[19, 20] The FROC curve is a tool for characterizing the performance of the proposed algorithm at all decision thresholds simultaneously.[28] The thresholds were decided by varying the number of the initial candidate in the detection step. The FROC curve was obtained by plotting the sensitivity as a function of the number of false positives per image (FPs/image). The sensitivity, which was defined as the number of TPs divided by the sum of TPs and false negatives (FN), indicated the ability of the algorithm to detect RNFL defects correctly. We defined the sensitivity and the number of FP per image in this evaluation as follows:

$$Sensitivity = TP/(TP + FN)$$

$$FPs/image = \frac{RFP}{N_{img}}$$

where RFP is the number of remaining false positives after application of the FP reduction method and N_{img} is the total number of images.

2.3. RESULTS

Validity of the Proposed CAD in Automated RNFL Detection

We tested 98 patients with 140 RNFL defects, including 9 patients with 9 images with papillomacular bundle defects. The distribution of the number of RNFL defects per case was as follows: 60 patients, single RNFL defect; 34 patients, 2 RNFL defects; and 4 patients, 3 RNFL defects. Among the 131 defects of 89 patients with glaucoma, the algorithm identified 117 defects and failed to identify 14. Among the 9 defects of 9 patients with papillomacular bundle defects, the algorithm identified all 9 defects. The results obtained by using the proposed algorithm are shown in Figure 2.6. The white arrows indicate the region of the RNFL defect marked by the 2 ophthalmologists and the yellow lines indicate the TPs. The first column shows the original images, the second column shows the correct detection results, and the third column shows the red-free fundus photographs of the original images.
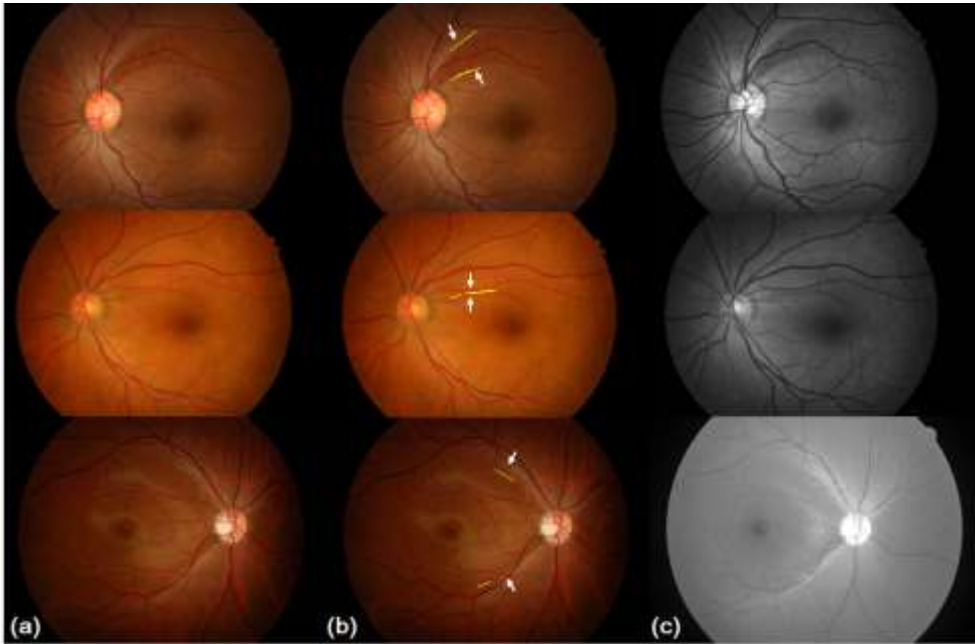
Figure 2.6 Representative detection results using the proposed algorithm on 3 patients consisting of a typical superior temporal retinal nerve fiber layer (RNFL) defect in glaucoma (top row), slit-like RNFL defect in early stage preperimetric glaucoma (middle row) and papillomacular bundle RNFL defect in a patient with Leber's hereditary optic neuropathy (bottom row). (a) First column: original image, (b) second column: detection results, (c) third column: red-free fundus image of original image. White arrows indicate the region of RNFL defect marked by two ophthalmologists.

The FROC curve of the proposed algorithm for the 98 patients was derived by varying the number of the initial candidates in the detection step (Figure 2.7). The sensitivity by using non-uniform illumination was 74% and the sensitivity after illumination correction was increased 1.2-fold from 74% to 90%. Finally, a sensitivity of 90% was obtained at 0.67 FPs per image. The 100 fundus photographs of healthy normal subjects showed a false positive (FP) rate of 0.25 per image. Finally, the overall diagnostic accuracy of the proposed algorithm for detecting RNFL defects among 98 patients and 100 healthy individuals was 86% sensitivity and 75% specificity.
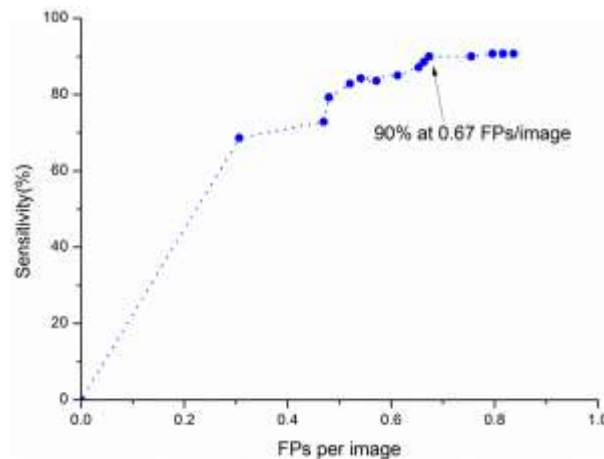
Figure 2.7 The free-response receiver operating characteristics curve indicating the performance of the proposed algorithm for detecting retinal nerve fiber layer defects. The proposed algorithm achieved 90% sensitivity at 0.67 false positives per image.

Intensity of RNFL Defects

In fundus photography, the intensity of the RNFL represents the thickness of the RNFL, and the thinning or loss of the RNFL appears as low intensity. Therefore, we compared the mean intensity of the blood vessel, RNFL defects, and normal RNFL region (Figure 2.8). In order to maintain the same grayscale level for each image, the grayscales of the images were normalized by using an arbitrary image. We automatically selected a region of interest (ROI) with a 50x50 square region in the 8 o'clock direction according to the clock-hour locations of figure 2.2, which was independent of eye orientation, at a distance of 100 pixels from the optic disc in the illumination corrected image. The ROI was set to minimize the effect of the darkened macula and RNFL defect region. The mean intensity of the normal RNFL region was calculated from the ROI excluding blood vessel region in the fundus image. The blood vessel region was selected in the same ROI and the mean intensity of blood vessel was calculated. The RNFL defect region was selected as an arbitrary region with the same size. The regions of the RNFL defects were marked by two ophthalmologists. The box plot shows the differences in the mean intensity. The mean intensity ($\pm$standard deviation) of the RNFL defects (38.20 ± 7.60) was significantly higher compared to the blood vessel region

(36.06 ± 7.19), but was lower compared to the normal RNFL region (40.20 ± 8.29) (F-value = 22.64, p < 0.005, by ANOVA).[20] Therefore, if the difference between the mean intensity of each candidate defect region and its surrounding background region is greater than the half value of the difference between the mean intensity of RNFL defects and normal RNFL, the candidate defect region was selected as an RNFL defect.
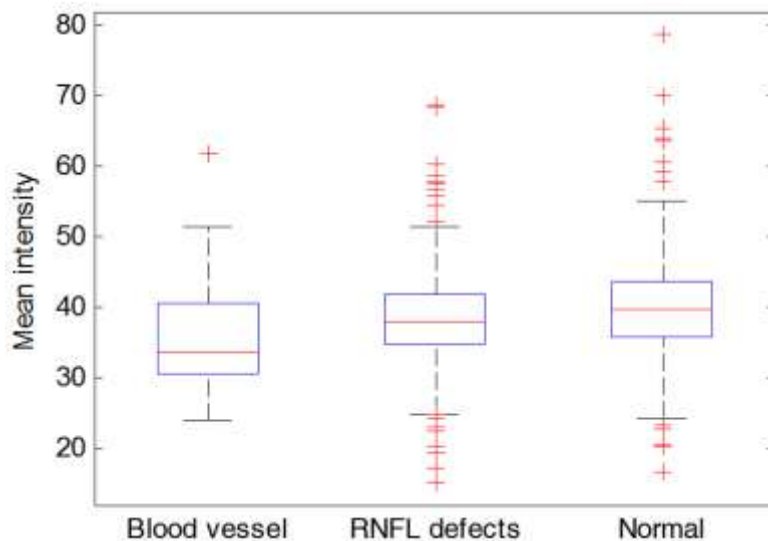
Figure 2.8 Mean intensity of the blood vessels, retinal nerve fiber layer (RNFL) defects, and normal RNFL regions. A central line of the box plot indicates the median value of the data. Lower and upper boundary lines of the central box are at the 25% and 75% quartile of the data. Box represents 95% confidence interval.

Location of RNFL Defects

The distribution of the clock-hour locations for the RNFL defects is shown in Figure 2.9. The RNFL defects were most frequently located at 7 o'clock, followed by 11 o'clock and 10 o'clock.
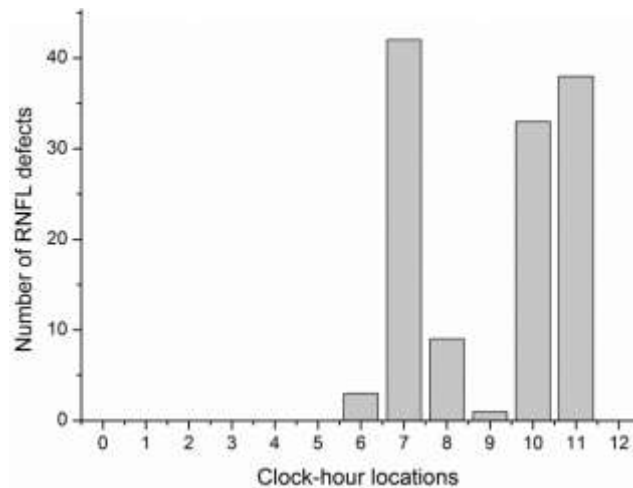
Figure 2.9 Distribution of clock-hour locations for the retinal nerve fiber layer defects.

Detection Rate According to Angular Widths of RNFL Defects

The detection accuracy as the angular widths of the RNFL defects increased is shown in Table 2.1. The angular width of the RNFL defects was defined as the angle between the proximal and distal border lines, with the height of each bar representing the true detection rate of the RNFL defects. Although the numbers of RNFL defects varied, the detection rates of the proposed algorithm were almost uniformly high, regardless of the angular widths of the RNFL

defects. The average detection accuracy was approximately 0.94.

Table 2.1 Performance of the proposed algorithm as a function of the angular widths of the retinal nerve fiber layer (RNFL) defects.

Angular Width(AW)	No. of RNFL Defects	True Positive	Detection Rate
10	30	26	87
20	37	33	89
30	26	22	85
40	19	18	95
50	9	9	100
60	3	2	67
70	6	6	100
80	3	3	100
90	1	1	100
110	1	1	100
120	2	2	100
130	1	1	100
140	2	2	100

2.4. DISCUSSION

In this study, we have proposed a fully automatic method for detecting various forms and widths of RNFL defects in color fundus images. Fundus photography is the most common screening tool to detect RNFL defects in various optic neuropathies. However, the detection of RNFL defects by using fundus photographs depends on the experience of the examiner, and early defects may be missed because of the low contrast of the RNFL. Therefore, we developed a simple and efficient algorithm to assist the ophthalmologist for the detection of RNFL defects.

The strength of the proposed algorithm is that it can detect very narrow defects in early stage glaucoma to non－glaucomatous optic neuropathy involving the papillomacular bundle accurately, as shown in the representative cases in Figure 2.6. To our knowledge, no previous studies described specific methods for detecting RNFL defects with various forms and widths in fundus images. Our results showed that the proposed algorithm was successful, with a sensitivity of 90% for glaucoma and 100% for papillomacular bundle defects in non－glaucomatous optic neuropathies.

Many algorithms have been proposed for detecting RNFL defects. Prageeth et al. used texture analysis by utilizing only intensity information about the RNFL around the optic disc in the

red-free fundus image.[21] Odstrcilik et al. proposed the use of texture analysis by utilizing Gaussian Markov random fields (GMRF) for classification of healthy and glaucomatous RNFL tissue in fundus images.[22, 23] These results were compared with the OCT images as a gold standard.[21, 22] Muramatsu et al. applied 3 sizes of Gabor filters to detect RNFL defects in the fundus image.[17] The detection rates were 89~91% at 1.0 FPs per image in these studies.[17, 22] However, because determining the filter width for detecting RNFL defects with various forms and widths is difficult with these methods, we applied the Hough transformation to detect RNFL defect candidates with straight continuous lines. In addition, these previous studies confined their study subjects to those with glaucoma with localized RNFL defects, which would be apparently visible and found on OCT; however, these studies did not include early stage preperimetric glaucoma, other non-glaucomatous optic neuropathies, and papillomacular bundle defects.

The RNFL defects were most commonly located in the inferior temporal and superior temporal regions. These locations are the most frequently affected in the early stage of glaucoma.[24] Additionally, the detection rate of the proposed algorithm was almost consistent, regardless of the angular widths of RNFL defects. However, among the total defects, the proposed algorithm

performed worse in cases with shallow defects, i.e., in early−stage glaucoma or in images with poor resolution.

This study had several limitations. First, the number of images used in this study was not large; thus, a larger database should be used in the future. Second, we did not consider structural changes of the optic disc, such as cupping, notching or pallor of the rim. Because the change in the optic disc is an important indicator of the severity of glaucoma, the detection of optic disc parameters can provide a significant differential clue regarding glaucomatous and non−glaucomatous optic neuropathies. [24, 25] Therefore, future work should be focused on the detection of optic disc changes, thereby combining these findings with RNFL defects. Further, regarding the high rate of false positives per image, modification of the FP reduction method may improve the reliability of the current algorithm for early detection of various optic neuropathies. Finally, diffuse RNFL defects in advanced glaucoma or optic atrophy cannot be detected with our program, since the mean intensity of the RNFL is low in all clock hours and a localized lesion is not distinguishable. However, in these cases, the pathologic features of disc cupping or atrophy are more prominent than RNFL thinning, and can easily be detected.

In conclusion, the proposed algorithm showed a reliable

diagnostic accuracy for automatically detecting RNFL defects in fundus photographs of optic neuropathy of various causes. This method has the potential to assist the ophthalmologist for double reading in the office and for mass screening by using fundus photographs.

Chapter 3. Automatic Computer-Aided Diagnosis of Optic Disc Pallor

3.1. INTRODUCTION

Optic disc pallor is a common clinical finding followed by axonal damage of the optic nerve. Optic disc pallor on fundoscopic examination is thought to be caused by changes in tissue translucency and reflectance following axonal loss and glial reorganization.[26] Assessment of the morphological characteristics of the optic disc including optic disc pallor, notching, cupping and edema together with the associated retinal findings is a critical step in making the correct diagnosis in patients with visual dysfunction.[27] However, optic disc morphology on fundus photographs can exhibit similar findings in various diseases, which makes it hard to distinguish between different etiologies solely based on morphological assessment.[27] In addition, there are certain conditions that may mimic pallor of the optic disc such as physiologic temporal pallor, pseudophakic eyes and myopic discs which are frequently misinterpreted as optic disc pallor in normal subjects during healthcare screening.[28] To discriminate these findings with true pallor of the optic disc related to pathologic axonal loss can be

extremely challenging, particularly if the pallor is mild and limited to the temporal aspect of the disc. The variable quality of brightness in fundus photographs makes it even perplexing to accurately detect optic nerve pallor.[29]

Despite the extensive use of quantitative imaging techniques such as optical coherence tomography (OCT) and Heidelberg Retinal Tomography (HRT) nowadays, most of the health care centers and primary eye care clinics use fundus photography as an initial screening tool for posterior segment eye diseases due to its cost−effective and feasible nature. The interpretation of fundus photographs in the common clinical setting rely on manual detection by an examiner, which is subject to interindividual variability.[27] Thus, to improve the accuracy of interpretation of fundus photographs, there have been previous attempts to assess optic disc pallor by objective and quantitative methods based mainly on color discrimination and manual or semi−automated measurements.[30−39] However, most of the previous studies used fundus cameras equipped with a special filter for assessing optic disc pallor on fundus photographs and the overall procedure was semi−automated requiring manually demarcated region of interests of the optic disc.[30−39] Herein, in this study, we developed a fully automated novel computer−aided detection (CAD) system for optic

disc pallor on fundus photographs via a risk analysis algorithm. We evaluated the performance of the system in differentiating subjects with normal optic discs and those with various degrees of optic disc pallor.

3.2. METHODS

Subjects and Fundus Photographs

We tested 230 photographs including 107 photographs with temporal and diffuse optic disc pallor, and 123 normal optic discs. Fundus photographs with optic disc pallor were recruited from 107 patients who were diagnosed with optic neuropathy, including hereditary causes such as autosomal dominant optic atrophy and Leber's hereditary optic neuropathy, and acquired causes of compression, inflammation, and idiopathic optic atrophy. The other 123 fundus photographs were collected from subjects who did not have any ocular diseases and featured normal appearance of the optic disc on fundus photographs. Fundus images were photographed as 24-bit color images using a digital SLR camera (Nikon D80; Nikon Co. Ltd., Tokyo, Japan) equipped with a fundus camera (KOWA VX-10; Kowa Company Ltd., Tokyo, Japan). Images were resized to a resolution of 1278x848 pixels.

The presence of optic disc pallor was classified according to the morphologic features of the optic disc on fundus photographs and was confirmed by Stratus® OCT (Carl Zeiss Meditec, Germany) or Spectralis® OCT (Heidelberg engineering, Germany) results showing retinal nerve fiber layer (RNFL) thinning by circumpapillary RNFL analysis as the gold standard test for determining optic disc pallor. Among the 107 photographs with optic disc pallor, 59 photographs were classified as having a relative temporal pallor, while 48 photographs showed diffuse pallor of the optic disc.

To compare the results of the CAD system with manual detection, two independent ophthalmologists determined the presence of optic disc pallor on fundus photographs. Each case was classified as having optic disc pallor when both reviewers agreed on the presence of optic disc pallor. When the readings of the two examiners were discrepant, the case was considered 'undetermined'. The accuracy of manual detection was compared with the diagnostic accuracy of the newly proposed CAD model.

Subjects with glaucomatous optic neuropathy, indistinguishable retinal images owing to media opacity such as corneal opacity, cataract, and abnormal retinal findings that obscure the detection of optic disc morphology such as macular

36

degeneration or retinal hemorrhage were excluded. The research was approved by the Institutional Review Board of Seoul National University Bundang Hospital and adhered to the tenets of the Declaration of Helsinki.

Analysis of Optic Disc Pallor

In this study, we proposed a risk analysis algorithm of optic disc pallor using a logistic regression model. The proposed algorithm consists of the following three steps; 1) automated detection of the optic disc boundary, 2) image enhancement, and 3) feature extraction from the neuroretinal rim for the logistic regression model.

Automated Detection of the Optic Disc

Optic disc segmentation is not quite simple because its size, color and the presence of peripapillary atrophy on fundus photographs vary greatly among subjects.[40] In this study, optic disc segmentation was automatically performed using a novel program that we developed using Matlab 2015b.[41] In our previous work, we proposed a method to detect the optic disc center in fundus photographs.[42] The image was then cropped to the size of 700x700

pixels with the optic disc center placed in the middle. Since the radius of the optic disc varies from 100 to 200 pixels in fundus photographs, the cropped size was chosen to be large enough to cover the whole optic disc area. Automatic segmentation of the optic disc was performed using a simple threshold method, and finally, the results of optic disc segmentation were confirmed by an ophthalmologist (HKY).

Image Enhancement

Image enhancement was performed according to the following three steps. First, we separated the green channel image (G) and blue channel image (B). The G image provides high contrast of blood vessels and optic disc structures. The B image is quite noisy, but provides a dark background that provides a high contrast of the optic disc. The G image was corrected (Gc) for noise reduction and illumination correction using the same methods that were used in our previous work regarding the automated CAD system for RNFL defects.[42] Then, we combined the corrected green channel image (Gc) and B image prior to analysis (Figure 3.1).
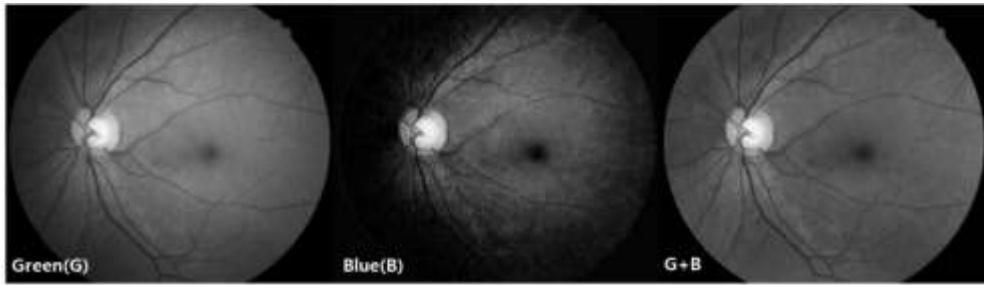
Figure 3.1 Examples of image enhancement for noise reduction and illumination correction. (a) Illumination corrected green channel image, (b) blue channel image, and (c) the combined image of corrected green channel image and blue channel image.

Feature Extraction

The morphological characteristics of optic disc pallor in fundus photographs are defined as the pale color of the neuroretinal rim, which gets brighter with disease progression in various optic neuropathies.[26, 34, 43, 44] The neuroretinal rim can be segmented by subtraction of the optic cup from the whole optic disc area. However, defining the boundaries of the optic cup solely on fundus photographs is not feasible.[27] Therefore, feature extraction for neuroretinal rim analysis was conducted in terms of a 'clinically significant neuroretinal rim' area that was defined as 5 consecutive pixels adjacent to the automatically segmented optic disc boundaries.[45] We measured the average brightness intensity of the 'clinically significant neuroretinal rim' area in all clock-hour

locations (Figure 3.2). The clock-hour locations were defined as follows; the nasal sector was defined as 2 to 4 clock-hour locations and the temporal sector was defined as 8 to 10 clock-hour locations.[42, 46]
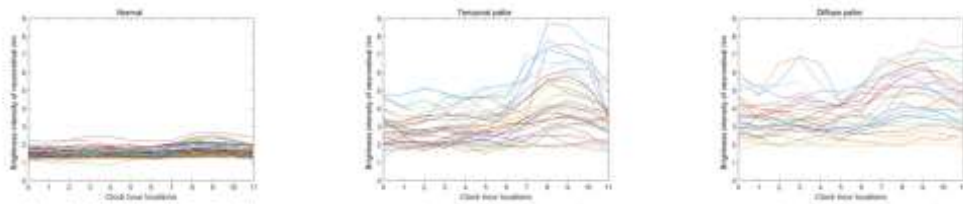
(a) normal   (b) temporal pallor   (c) diffuse pallor

Figure 3.2 Average brightness intensity profiles of the clinically significant neuroretinal rim area in all clock-hour locations for each case of (a) normal subjects, (b) temporal pallor of the optic disc and (c) diffuse optic disc pallor.

Parameters of Optic Disc Pallor

Two parameters were developed for risk analysis of optic disc pallor; 1) Brightness correction ratio (BC) and 2) Temporal-to-nasal ratio (TN) were generated by an automatic algorithm using fundus photographs and manually segmented masks of the optic disc. The brightness of color fundus photographs is not uniform owing to non-ideal acquisition by different fundus cameras and illumination

conditions.[29] Therefore, to correct the brightness of the image, BC was defined as the ratio of the mean brightness intensity of the 'cup depth' compared to the 'background region'. The 'background region' was defined as a square in the papillomacular bundle nerve fiber layer (Figure 3.3). The center of the background region was automatically set at one–disc diameter apart from the geometric center of the optic disc. The height of the background region was fit within ±10 degrees from the geometric center of the optic disc and the width was fixed at 15 pixels. The brightness intensity of the 'cup depth' was calculated as the mean intensity of pixels that had a higher intensity than 70% of the maximum value in the optic disc area. TN was defined as the mean brightness intensity of pixels in the temporal region divided by the mean intensity of pixels in the nasal region of the clinically significant neuroretinal rim.
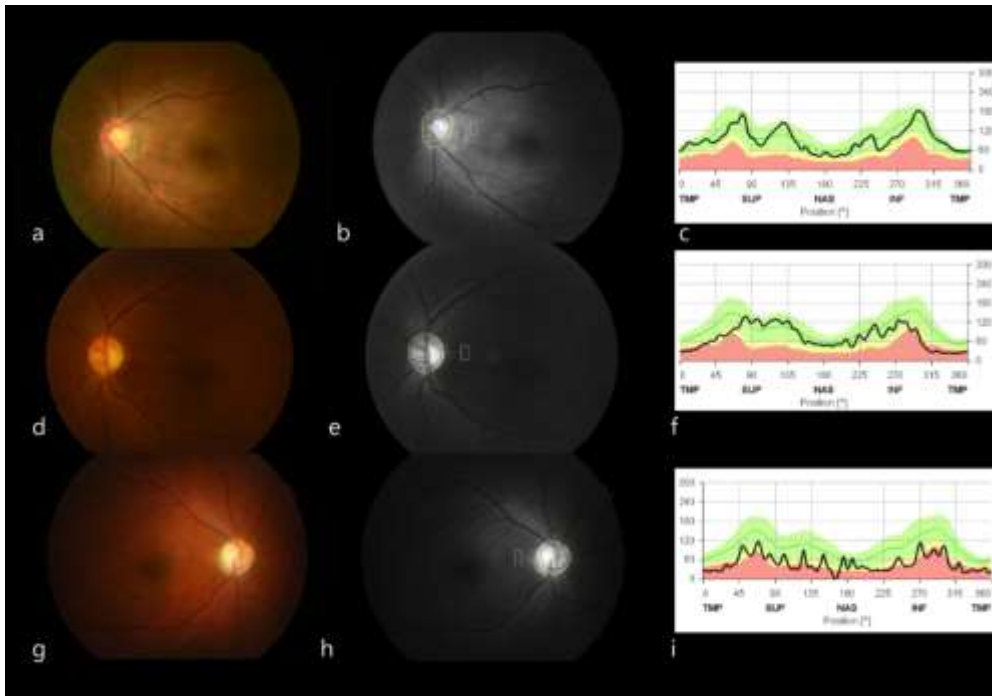
Figure 3.3 Representative fundus photographs, segmentation results of the CAD model and circumpapillary RNFL thickness map in (a-c) normal subjects, (d-f) temporal pallor of the optic disc and (g-i) diffuse pallor. The background region (white square) was set at the papillomacular nerve fiber bundle to adjust for inconsistent brightness of color fundus photographs. Fully automated segmentation of the boundaries of the optic disc and clinically significant neuroretinal rim (area between the yellow and black circle) were depicted. The proposed CAD model calculated the risk of optic disc pallor within the clinically significant neuroretinal rim area.

Statistical Analysis

Comparison of BC and TN values between groups were performed using one-way ANOVA and when statistical significance was identified, post-hoc analysis was carried out with the Tukey's test. For the risk analysis of optic disc pallor, we used a logistic regression model with the two parameters of optic disc pallor, BC and TN, as continuous variables. All tests were performed using the SPSS version 20.0 software package (SPSS Inc., Chicago, IL). A P-value of less than 0.05 was considered as statistically significant. The general form for the logistic regression model is,

$$\text{logit}(P) = \beta_0 + \beta_1 X_1 + \beta_2 X_2 + \cdots + \beta_n X_n$$

where P is the probability, X is the feature, and β is the coefficient of the model.[47] The logistic regression model was trained to obtain predicted probabilities of the risk of optic disc pallor. The two features entered the logistic regression model when variance inflation factors (VIF) were less than 10. The VIF was defined as a degree of collinearity present for each factor and a VIF greater than 10 indicates significant multicollinearity. The regression model yielded estimated regression coefficients that weighted the information from the two features in an optimal way for combining them. In this study, two parameters indicating optic disc pallor, BC and TN, were generated by the automatic algorithm using fundus

43

photographs and manually segmented mask of the optic disc. The regression analysis also determined whether each variable was significantly associated with the probability of optic disc pallor. The overall predictive ability of the proposed model was evaluated by use of the area under the receiver operating characteristic (ROC) curve (AUC). [48, 49] The sensitivity, specificity and accuracy of this model were calculated as follows.[50]

$$\text{Sensitivity} = \frac{Number\ of\ pallor\ cases\ correctly\ predicted\ (N_{TP})}{Total\ number\ of\ pallor\ cases\ in\ sample\ (N_A)}$$

$$\text{Specificity} = \frac{Number\ of\ normal\ cases\ correctly\ predicted\ (N_{TN})}{Total\ number\ of\ normal\ cases\ in\ sample\ (N_N)}$$

$$\text{Accuracy} = \frac{(N_{TP} + N_{TN})}{(N_A + N_N)}$$

3.3. RESULTS

Parameters of Optic Disc Pallor

Linear regression analyses demonstrated that BC (β = 0.892; P = 0.0001) and TN (β = 0.123; P = 0.033) were significantly different between normal subjects and those with optic disc pallor.

The mean value of BC in normal subjects was significantly lower (1.94±0.42) than those with temporal pallor (5.41±1.90, P<0.001) and diffuse pallor (5.28±1.70, P<0.001) (Figure 3.4a). There was no significant difference in BC values between subjects with temporal pallor and diffuse pallor (P=0.870).

The mean value of TN in normal subjects was significantly lower (1.12±0.15) than those with temporal pallor (1.51±0.52, P<0.001), but not significantly different with diffuse pallor (1.24±0.22, P=0.072) (Figure 3.4b). TN value was significantly higher in subjects with temporal pallor compared to diffuse pallor (P<0.001).
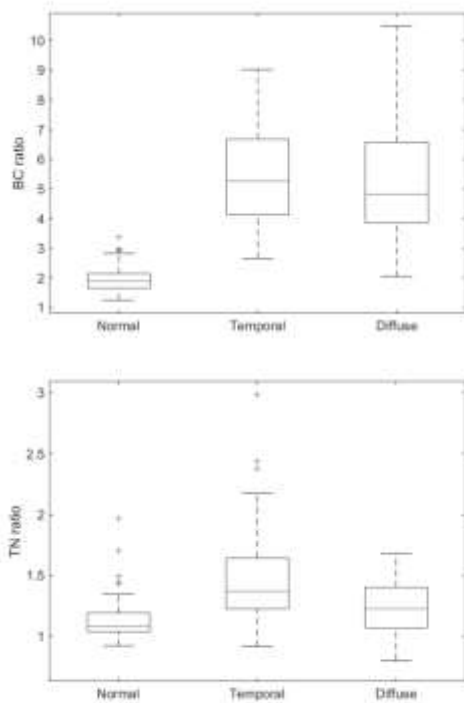
Figure 3.4 Box plots of the Brightness correction ratio (BC) and Temporal-to-Nasal area ratio (TN) for normal subjects and those with optic disc pallor. A center line of the box indicates the median value of data. Lower and upper boundary lines of the box are the 25 ro 75% quartile, and marginal lines represent 95% confidence interval.

Risk Analysis of Optic Disc Pallor

A linear model was created to associate the risk of optic disc pallor with the two parameters, BC and TN, to generate a probability map. Based on the results of this model, we obtained the following

equation for the probability (P) of optic disc pallor.

$$\text{Logit}(P) = -27.695 + 5.429 * BC + 13.122 * TN$$

The probability of optic disc pallor ranged from 0 to 1, and the risk of having optic disc pallor was higher with a value closer to 1. The P value for each coefficient in the final model was significant (P value for the constant, BC, and TN were <0.0001, 0.0001 and 0.022, respectively). Higher risk of optic disc pallor was significantly associated with a larger BC (P<0.001) and TN (P=0.022).

Accuracy of CAD for Optic Disc Pallor

The probability of optic disc pallor by the linear regression model with BC and TN was used to generate the ROC curve (Figure 3.5). A probability value of 0.5 or more was used as the cutoff value of detecting optic disc pallor in fundus photographs using the linear regression model. Our results showed that the proposed model successfully detected optic disc pallor among normal patients with a sensitivity of 95.3% and a specificity of 96.7%. The accuracy was 96.1% and AUC value was 0.996.

Comparing the results of manual detection by two independent ophthalmologists, 13.9% (32/230) of cases were 'undetermined' due to inconsistent results between the two

examiners. Disagreement between both examiners was found in 8.1% (10/123) of normal subjects, 22.0% (13/59) of temporal pallor, and 18.8% (9/48) of diffuse pallor. The accuracy of the results of individual examiners were 90.0% and 94.8%, respectively.
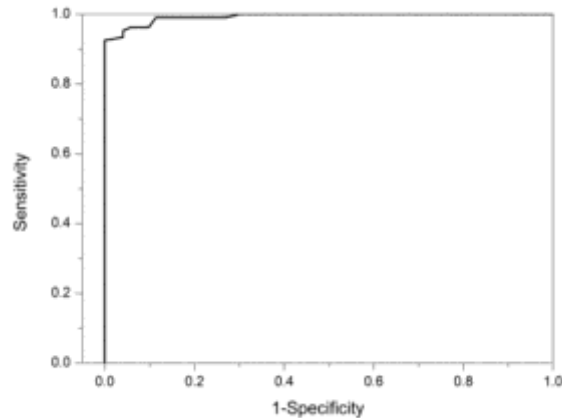
Figure 3.5 ROC curve of the proposed model for detecting optic disc pallor. The performance of the proposed CAD model for detecting optic disc pallor in 230 fundus photographs of 123 normal subjects and 107 subjects with optic disc pallor achieved a sensitivity of 95.3% and specificity of 96.7% (AUC=0.996).

After excluding undetermined cases, the sensitivity of manual detection was 98.9% and specificity was 99.1% for diagnosing optic disc pallor among the 198 cases (86.1%) that were interpreted identically by the two examiners. When 'undetermined' cases were reclassified as having optic disc

pallor, the specificity dropped to 91.1% with a sensitivity of 99.1%. Two cases were erroneously judged as having optic disc pallor or a normal optic disc by both examiners, whereas they were accurately diagnosed with the proposed CAD model.

3.4. DISCUSSION

In this study, we developed a fully automatic CAD system for detecting variable degrees of optic disc pallor on color fundus images by a risk analysis model generated by novel parameters. The proposed model showed a relatively good performance in detecting both diffuse and temporal optic disc pallor caused by various etiologies with a sensitivity of 95.3% and specificity of 96.7%. The accuracy of the CAD model was superior to the results of manual detection by individual examiners.

The strength of the proposed algorithm in our study is as follows. First, our CAD system detected optic disc pallor through a fully automated process, beginning with optic disc segmentation to the final step of providing a probability score of optic disc pallor by a risk analysis model. Second, the combination of corrected green channel images and blue channel images provided a high contrast of the optic disc compared to previous studies on quantitative assessment of optic disc pallor.[32-39] Third, we adopted two novel

concepts to overcome the major obstacles of objective assessment of optic disc pallor in previous studies.[32-39] Due to the difficulty in delineating the boundaries of the optic cup and neuroretinal rim area on fundus photographs, we defined a 'clinically significant neuroretinal rim' adjacent to the optic disc boundary that can be automatically segmented without difficulty.[45] In addition, the variable quality of brightness in fundus photographs acquired by different fundus cameras and illumination conditions[29] was adjusted using the Brightness correction ratio (BC). Fourth, the inclusion of 'TN ratio' as a parameter of the risk analysis model effectively detected temporal pallor of the optic disc which is often confused with physiologic temporal pallor of the disc in normal subjects. Finally, be verified the results of CAD using OCT as the gold standard method instead of manual detection which is subject to interindividual variability. In fact, the CAD system showed relatively superior results compared to individual manual detection of optic disc pallor on fundus photographs.

There have been previous attempts to measure optic disc pallor on fundus photographs.[30-39] Zenker et al.[30] introduced a photographic technique using green and red filters taken simultaneously at different angles by a stereoscopic fundus camera, and the pallor-disc ratio was calculated in black and white films.

Sorenson[31] took fundus photographs using a purple filter, and the difference between the blue and red density was used to determine optic disc color with the normal optic disc reflecting red light and pale disc reflecting blue light. Miller et al.[32] undertook videographic imaging of the optic disc (Rodenstock Analyzer) that was consecutively taken under green (540 nm) and red (640 nm) illumination at different time points to quantify optic disc pallor in a small number of patients with glaucoma. Vilser et al.[33] described a method using a special dual bandpass filter (548 and 610 nm) mounted on a fundus camera to simultaneously obtain red and green images of the optic disc to determine a mean pallor value. This method was applied in a recent study by Ramm and colleagues[51] to quantitatively assess optic disc pallor in 89 patients with primary open angle glaucoma (POAG), which showed a higher value of pallor in POAG compared to healthy normal subjects. Unfortunately, these studies all required a special filter while taking fundus photographs to obtain an ideal image for assessing optic disc color, which is not the usual case in regular clinical practice.

Quantitative measurement of optic disc pallor on fundus photographs without using a special filter also have been reported.[34, 37] However, the previous studies mainly relied on color discrimination of red, green and blue pixels using common image

analysis software, which employed calculation algorithms using the mean intensity of each color to quantify optic disc pallor.[34] Conversely, in our study, the combination of corrected green channel images and blue channel images provided a high contrast of the optic disc compared to the former studies which allows accurate segmentation and color discrimination of the optic disc. Moreover, the former methods were not fully automated as the region of interests including the border of the optic disc was manually demarcated on digital color fundus photographs.[11,14] Fully automated segmentation of the optic disc with high accuracy, as in our study, is essential for image analysis and preprocessing particularly in the era of deep learning which has a promising potential for screening and diagnosis in the near future.[52]

Variability in the brightness of fundus photographs is one of the major issues that decrease the reproducibility of manual interpretation or image analysis.[29, 53, 54] Our new algorithm was based on the knowledge that assessment of optic disc pallor may vary according to the luminance and image quality of fundus photographs.[29, 53] While a standardized method of image acquisition and enhancement has been recommended for best quality images to detect retinopathies,[29] the best parameters for assessing optic disc color have not been thoroughly evaluated.[34, 54] In our study, the

mean brightness intensity of the background region was calculated in the papillomacular nerve fiber bundle, which is not interrupted by vessels and located close to the visual axis of which the luminance is least affected by pupil size. By adopting the BC ratio in our CAD model, fundus photographs with variable quality and luminance were effectively analyzed with excellent accuracy.

In our study, we introduced a novel parameter, the TN ratio that was automatically calculated to detect temporal optic disc pallor. Segmental pallor of the optic disc cannot be detected by simply calculating mean values of optic disc pallor unless multiple regions are assessed separately or the region of suspected pallor is delineated by the examiner.[11,14] The TN ratio in this study allowed automatic detection of relative temporal pallor by the CAD system with a sensitivity of 94.9% and specificity of 95.1%, and no additional steps were required. In a previous study regarding the accuracy of morphological assessment of the optic disc by glaucoma and neuro−ophthalmology experts, a major disagreement between examiners was found on determining the presence of optic disc pallor in autosomal dominant optic atrophy and Leber's hereditary optic neuropathy.[27] This implies that manual detection of temporal pallor is extremely unreliable even among experts, and the results attained in this study indicate the superiority of our

proposed CAD system in optic disc pallor detection over subjective interpretation.

There are certain limitations in our study. First, the reproducibility of the CAD system could not be determined by multiple photographs taken from one person as this was a retrospective study and most of the subjects had only one fundus photograph taken at each examination. Second, our study did not include subjects with glaucomatous optic neuropathy. Moderate to severe glaucoma or widespread chorioretinal disease may also end up with secondary optic disc pallor in advanced stages.[51, 55] Therefore, differentiation of optic disc structure between glaucomatous optic neuropathy and compressive optic neuropathy may be confusing particularly in advanced stages.[34, 51, 55] While optic disc pallor is considered the most crucial difference between glaucoma and compressive optic neuropathy, even glaucoma may exhibit some degree of pallor compared to healthy controls which complicates the matter.[51] Nakano et al.[34] showed that the redness of the neuroretinal rim was effective in differentiating mild stages of compressive optic neuropathy and normal tension glaucoma. However, the diagnostic performance of their color index was not impressively high with an AUC of 0.7. Therefore, future studies to differentiate glaucoma and non−glaucomatous optic neuropathy

among normal optic discs should be performed to enhance the utility of the software in mass screening. In this case, other morphological features of the optic disc such as cupping or notching of the rim, together with the detection of RNFL defects should be combined.[42] Finally, our CAD system should be validated in different ethnicities as the brightness of the background region may partly depend on the degree of choroidal pigmentation.

In conclusion, we developed a fully automated CAD system to detect optic disc pallor in fundus photographs that can assist the ophthalmologist with making clinical judgements. Our model showed excellent performance in assessing both diffuse and temporal optic disc pallor, and the accuracy of the CAD model was superior to individual manual detection.

Chapter 4. Efficacy of Automated Computer-Aided Diagnosis of Retinal Nerve Fiber Layer Defects in Healthcare Screening

4.1. INTRODUCTION

Glaucoma is one of the leading causes of blindness worldwide.[56] A meta-analysis study recently showed that the global prevalence of glaucoma for population aged 40-80 years was estimated to be 3.54%.[57] Asians account for almost half of the world's total glaucoma cases,[58] and population-based studies revealed that the prevalence of primary open-angle glaucoma in the population of 40 years or older was 3.5% in Korea and 3.9% in Japan.[59, 60] Glaucoma can remain asymptomatic until very advanced stages, which leads to a high prevalence of undiagnosed glaucoma in up to 50% of affected people.[61] As glaucoma decreases vision-related quality of life even in earlier stages of the disease and causes irreversible damage to the optic nerve, early detection is important.[62] A variety of studies highlight the high prevalence of undiagnosed glaucoma, pointing to the need for devising new screening strategies to identify these individuals and assure they receive proper care.[61, 62] Application of a

technology-based first assessment might be a cost-effective option for improving the performance of testing for glaucoma detection.[63]

Structural changes of glaucoma are represented by alteration of the optic nerve head configuration and retinal nerve fiber layer (RNFL) defects.[64] Localized RNFL defects indicate optic nerve damage with a specificity of more than 90 %,[65] although these are not pathognomonic for glaucoma.[66] . Localized RNFL defects can be the first structural sign of glaucoma before enlargement of the optic cup,[67] and can also be seen before the development of apparent visual field loss.[68, 69] Thus, detection of localized RNFL defects can be one of the most effective methods for early glaucoma screening.

Detection of RNFL defects is also important in the diagnosis of non-glaucomatous optic neuropathies.[1, 2] As papillomacular RNFL bundle (PMB) defect is one of the major signs of various hereditary, toxic and mitochondrial optic neuropathies, early detection of PMB defects can enable the diagnosis of systemic optic neuropathies at an earlier stage of the disease.[1, 2]

To detect RNFL defects, fundus photographs, optical coherence tomography and scanning laser polarimetry have been used.[9, 70-78] Although the latter two tests enable the acquisition of 3D imaging and determine the actual thickness of RNFL, those are

costly and time-consuming,[7] thus are less suitable for mass screening of glaucoma compared to fundus photographs.[8] Development of techniques for automatic detection of RNFL defects is important for glaucoma screening using fundus photographs in a large population, and several researches have been performed for the development of the techniques.[17, 78-80]

In our previous work, we developed a new system for automatic computer-aided detection (CAD) of RNFL defects using fundus photographs, and showed its high sensitivity in detecting glaucomatous and non-glaucomatous optic neuropathies.[42] In the present study, we evaluated the validity of the new CAD system in mass screening of RNFL defects using fundus photographs in a large population from a single healthcare center.

4.2. METHODS

Study Population

This study included fundus photographs of 1200 patients who visited the Health Promotion Center of Seoul National University Bundang Hospital from July, 2013 to August, 2014. Fundus photographs were taken as 24-bit color images by using the digital camera (D80, Nikon, Tokyo, Japan) equipped with a fundus camera

(VX-10, Kowa, Tokyo, Japan), and then were resized with a resolution of 1278 × 848 pixels. The exclusion criteria were as follows: (1) Phthisis or anophthalmos (2) Indistinct retinal image due to media opacity including cataract or corneal opacity (3) Abnormal retinal findings that might disrupt the detection of RNFL defect, such as macular degeneration, diffuse retinal hemorrhage or macular edema. After excluding the cases inappropriate for analysis, 2270 fundus photographs were included. This study was conducted in compliance with the Declarations of Helsinki and was approved by the Institutional Review Board (IRB) of Seoul National University Bundang Hospital.

Manual detection of RNFL Defect

The fundus photographs were reviewed independently by two expert ophthalmologists (S.B.H and H.K.Y) for detection of RNFL defects, in the same manner as in the previous study.[27] When both reviewers determined the presence of an RNFL defect, the case was considered to have an RNFL defect. The results of manual detection were considered as the gold standard.

Automatic Detection of RNFL Defect using CAD Method

Automatic determination of RNFL defect using CAD was performed in the same manner as in our prior study.[42] Briefly, the color fundus photographs were converted to green channel images to maximize the contrast between the RNFL defects and blood vessels.[10] The images were pre-processed for reduction of noise by applying a binary mask and a median filter. Correction of the non-uniform illumination was performed for accurate blood vessel segmentation by enhancing the contrast of the blood vessels at the periphery of the fundus photographs.[11] After that, blood vessel removal was done to detect RNFL defects more accurately. The blood vessels were extracted by using a morphological bottom-hat transform in order to detect the blood vessels as dark regions, as previously described.[42] For exact extraction of the entire blood vessel structure, the Kirsch method in which an edge detector was used to determine the maximum edge strength was also applied.[15] After blood vessel removal, the image was transformed to polar coordinates in regard to the center of the optic disc to detect RNFL defects effectively. In polar coordinates, a point is expressed by a radial distance and the angle from the optic center. Hence, candidates of RNFL defect were transformed to a straight line in the

vertical direction because the defects appear radially from the optic disc center. Subsequently, the polar transformed image was filtered with 2D Gaussian filter for smoothening blood vessel boundaries, and the edge of the image was determined using the Canny edge detection algorithm.[81] Hough transformation for line detection was then applied to detect the candidates of RNFL defect. To reduce false-positive (FP) rate, knowledge-based rules were applied to discern misdetected RNFL defect candidates. For each candidate, the average pixel numbers, the vertical length and the angular location of the candidate region were documented. Using these 3 parameters, the misdetected candidates of RNFL defect were eliminated according to reference values established in our prior study, and only true candidates of RNFL defects remained. Because the RNFL does not spread out in complete radial directions around the optic disc center, the polar transformation image of RNFL defect lines are slightly tilted toward the macula. In this study, to reduce FP rate, we selected only the defect candidates tilted toward the macular position. In addition, we also limited the angular range in inverse proportion to the radial distance from the optic disc center.

Evaluation of the Efficacy of the CAD System

To determine the performance of the CAD method quantitatively, a free-response receiver operating characteristics (FROC) curve was derived by varying the angular range and threshold of detection. The FROC curve is generated by plotting the sensitivity as a function of the number of FPs per image (FPs/image) that was calculated by dividing the number of remaining FPs after application of varying methods by the total number of images. The point of minimum FPs/image at which sensitivity does no more increased was determined. The results of automatic detection of RNFL defects using CAD at the minimum point of FPs/image was compared to those of gold standard manual detection for evaluation of the sensitivity and specificity of the CAD method. SPSS software for Windows (V.18.0; SPSS Inc.) was used for statistical analyses.

4.3. RESULTS

Of the 2400 fundus photographs of 1200 subjects (M: F = 703:497), 130 photographs considered inappropriate for the analysis were excluded. Finally 2270 fundus photographs were used for the analyses. The mean age of subjects was 49.4 ± 9.9 years (range, 17-81 years of age).

Efficacy of the CAD System in Automated RNFL Detection

In manual detection that was considered as "gold standard", there were 36 eyes from 28 patients with at least one RNFL defect. Among the 36 eyes, 31 eyes had one localized RNFL defect and 5 eyes had two RNFL defects, adding up to a total of 41 RNFL defects. In the FROC curve of the automated detection using the CAD system to detect the 41 RNFL defects, a sensitivity of 90.2% (37 out of 41 RNFL defects) was obtained at a FP rate of 0.36 FPs/image, and no further improvement of the sensitivity was found with increasing FPs/image (Figure 4.1). At the FP rate of 0.36 FPs/image, specificity of the CAD system was 72.5%; 1620 photographs were correctly determined among the 2234 photographs with no RNFL defects, while 614 photographs were falsely detected to have an RNFL defect.
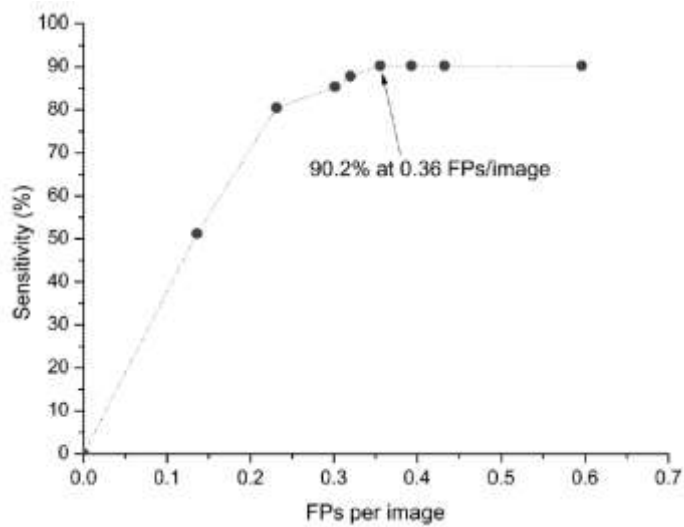
Figure 4.1 A free-response receiver operating characteristics (FROC) derived by plotting the sensitivity as a function of the number of FPs per image (FPs/image). The CAD system showed sensitivity of 90.2% at 0.36 FPs/image, and no further improvement in sensitivity with increase in FPs/image was found.

It took approximately 6 hours to analyze the 2270 fundus photographs, excluding the time spent for transferring the images to the system, which is about 9.5 seconds per image for detection of RNFL defects using this protocol.

4.4. DISCUSSION

Fundus photography is currently used as one of the major tools of health screening worldwide because it is technically easy and inexpensive. Studies suggested that RNFL analysis using fundus photographs can be a method for glaucoma screening.[70, 78, 82] Application of technology-based first assessment to automatically detect RNFL defects might be an option for improving glaucoma detection in a large population.[63]

There have been a few studies concerning techniques for automatic detection of RNFL defects in fundus photographs, and several algorithms have been proposed.[17, 23, 79, 80] Prior studies used texture analysis applying intensity information around the optic disc, analysis using the Gaussian Markov random fields or detection using three sizes of Gabor filters, showing detection rates of 89 to 91% at 1.0 FPs/image.[17, 23] However, these methods have limitations as follows: 1) despite the high sensitivity in detecting RNFL defects, these tests also showed high FP rates and low specificities, which limit its availability as screening tools, 2) filter width had to be pre-determined for each RNFL defect of various forms and widths, which is difficult and cumbersome, and finally, 3) although these methods could detect distinct RNFL defects that are

apparently visible on fundus photographs, it did not account for small defects in early stage preperimetric glaucoma or defects caused by non–glaucomatous optic neuropathies such as PMB defects.

In our previous study, we proposed a new method for defection of RNFL defect that showed a sensitivity of 90% with 0.67 FPs/image of by applying knowledge–based rules to filter out misdetected RNFL defect candidates.[42] The protocol could accurately detect RNFL defects with a narrow angle or PMB defects by adopting polar transformation, Canny edge detection algorithm and Hough transformation for line detection.

In the present study, we upgraded our CAD protocol to enhance the specificity and reduce FP rates by selecting only the candidates of RNFL defects tilted toward the macular position and limiting the angular range in inverse proportion to the radial distance from the optic disc center. To investigate whether the new method can be used in mass screening of RNFL defect in a large population, we tested the sensitivity and specificity of the protocol for detection of RNFL defects using 2270 fundus photographs in the database of a health promotion center at our hospital. The CAD system demonstrated a sensitivity of 90.2% and specificity of

72.5% at 0.36 FPs/image, which is better than the results of the previous studies.[17, 23] The speed of analysis may not be faster than experienced ophthalmologists or trained examiners. However, we believe that our CAD system can facilitate mass screening by saving the burden of ophthalmologists as a first assessment screening tool for filtering photographs with suspected RNFL defects. We also believe further studies are needed to enhance the speed and specificity of image analysis using the CAD system.

One of the major limitations of automatic detection systems of RNFL defects is that increasing its sensitivity inevitably leads to high FP rates. Nonetheless, high sensitivity cannot be sacrificed for a mass screening test because detection of every abnormality without omission is essential at the stage of screening and falsely detected samples can be eliminated at a secondary examination by an ophthalmologist. However, excessively high FP rates decrease the efficiency of the screening test and fail to alleviate the burden of ophthalmologists. Thus, efforts should be made to improve specificity without sacrificing sensitivity. In the present study, we developed a new CAD system that showed a sensitivity of > 90% with improved specificity at only 0.36 FPs/image, which increased the feasibility of our CAD system as an effective screening protocol of RNFL defects. Further studies are warranted for improvement of

the efficacy of the CAD system, and ultimately, for the development of an ideal system that can confirm the detection of RNFL defects without requiring secondary examination by an ophthalmologist.

The present study has limitations as follows. First, we did not evaluate the structural changes of the optic disc, which is an important sign in both glaucomatous and non-glaucomatous optic neuropathy.[17] Localized RNFL defects are not pathognomonic for glaucoma,[66] and were reported to be detected in 20-87% of glaucomatous eyes depending on the type of glaucoma.[65, 83] Nevertheless, despite the fact that detection of localized RNFL defects without evaluation of optic disc damage may not be an ideal screening test for glaucoma, it is useful for detecting other eye diseases. Moreover, our software cannot detect diffuse RNFL loss in advanced glaucoma or optic atrophy.[42] In these cases, prominent changes of the optic disc are more easily detectable. With further development of a protocol that can automatically locate the optic disc and analyze structural changes, we believe that the diagnostic ability can be improved by combining the findings of the optic disc and RNFL defects.[24, 25] Second, although our protocol may be useful in Asians, its efficiency in other races with different color fundi has not been evaluated. Further studies are needed for the establishment of diagnostic thresholds of the CAD system before it

can be applied in patients with other ethnicities. Third, a FP rate of 0.36 FPs/image is still unsatisfactory, although it has been improved compared to 0.67 FPs/image in our previous study.[42] Specificity of 72.5% is also insufficient for a mass screening test. The low specificity may cause unnecessary worry to the screened subjects. It can also lower the cost-effectiveness of the screening test by causing unnecessary further tests for glaucoma. Therefore, we believe further studies to achieve higher specificity without sacrificing sensitivity are necessary. An alternative method is to teach the photographers to do primary screening at the time the image is taken. However, this is also subject to individual variability of assessment, which can be decreased by objective examination using a computer software. Practically, this is not possible in many centers and additional reading is required by physicians. Finally, the repeatability and variability of the CAD system could not be determined because only one fundus photograph was taken for each patient. With the same photograph, the results of the CAD system are always identical. However, there can be slight discrepancies in brightness degree and saturation of fundus photographs between photographs taken on different days by different fundus cameras, and these conditions may affect the results of the CAD system.

In conclusion, the present study verified the accuracy of our

new CAD system for the detection of RNFL defects in mass screening with high sensitivity and specificity. With further refinement, we believe our CAD system can be widely used in healthcare screening centers and alleviate the burden of ophthalmologists.

Chapter 5. Conclusion

Fundus photography is the most common screening tool to detect optic disc abnormalities in various optic neuropathies. In this study, we have proposed a fully automatic method for detecting morphological abnormalities of the optic disc in digital color fundus images. We developed a simple and efficient CAD algorithm to assist the ophthalmologist for the detection of RNFL defects and optic disc pallor. The proposed algorithm showed a reliable diagnostic accuracy for automatically detecting RNFL defects and optic disc pallor in optic neuropathies of various causes. Moreover, the accuracy of the CAD model for detecting optic disc pallor was even superior to the results of manual detection by individual examiners. Finally, validation of our model for detection of RNFL defects in healthcare screening showed high sensitivity and specificity. With further refinement and combination with deep learning algorithms, we believe that our CAD system can be widely used for automated first assessment in healthcare screening and primary eye care centers.

Bibliography

1.   Barboni P, Carbonelli M, Savini G, et al. Natural history of Leber's hereditary optic neuropathy: longitudinal analysis of the retinal nerve fiber layer by optical coherence tomography. Ophthalmology 2010;117(3):623-7.

2.   Wang MY, Sadun AA. Drug-related mitochondrial optic neuropathies. J Neuroophthalmol 2013;33(2):172-8.

3.   Hwang JM, Kim TW, Park KH, et al. Correlation between topographic profiles of localized retinal nerve fiber layer defects as determined by optical coherence tomography and red-free fundus photography. J Glaucoma 2006;15(3):223-8.

4.   Haleem MS, Han L, van Hemert J, Li B. Automatic extraction of retinal features from colour retinal images for glaucoma diagnosis: a review. Comput Med Imaging Graph 2013;37(7-8):581-96.

5.   Hoh ST, Greenfield DS, Mistlberger A, et al. Optical coherence tomography and scanning laser polarimetry in normal, ocular hypertensive, and glaucomatous eyes. Am J Ophthalmol 2000;129(2):129-35.

6.   Cheng J, Liu J, Xu Y, et al. Superpixel classification based optic disc and optic cup segmentation for glaucoma screening. 2013.

7.   Lu CK, Tang TB, Laude A, et al. Quantification of parapapillary atrophy and optic disc. Invest Ophthalmol Vis Sci 2011;52(7):4671-7.

8.   Nduaguba C, Lee RK. Glaucoma screening: current trends, economic issues, technology, and challenges. Curr Opin Ophthalmol 2006;17(2):142-52.

9.   Kim TW, Park UC, Park KH, Kim DM. Ability of Stratus OCT to identify localized retinal nerve fiber layer defects in patients with normal standard automated perimetry results. Invest Ophthalmol Vis Sci 2007;48(4):1635-41.

10.   Khalid NEA, Noor NM, Mahmud Z, et al. Bridging quantitative and qualitative of glaucoma detection. World Academy of Science, Engineering and Technology 2012;72.

11.   Kubecka L, Jan J, Kolar R. Retrospective illumination correction of retinal images. Int J Biomed Imaging 2010;2010:780262.

12.   Youssif AA, Ghalwash AZ, Ghoneim AS. Comparative study of contrast enhancement and illumination equalization methods for retinal vasculature segmentation. Proc Cairo Int Biomed Eng Conf 2006.

13.   Kolar R, Odstrcilik J, Jan J, Harabis V. Illumination correction and contrast equalization in colour fundus images. 19th

European signal processing conference (EUSIPCO 2011) Barcelona, Spain 2011.

14.   Zheng Y, Vanderbeek B, Xiao R, et al. Retrospective illumination correction of retinal fundus images from gradient distribution sparsity. Biomedical Imaging (ISBI), 2012 9th IEEE International Symposium on: IEEE, 2012.

15.   Karasulu B. Automatic extraction of retinal blood vessels: a software implementation. European Scientific Journal 2012;8(30).

16.   Fraz MM, Basit A, Barman S. Application of morphological bit planes in retinal blood vessel extraction. Journal of Digital Imaging 2013:1−13.

17.   Muramatsu C, Hayashi Y, Sawada A, et al. Detection of retinal nerve fiber layer defects on retinal fundus images for early diagnosis of glaucoma. J Biomed Opt 2010;15(1):016021.

18.   Zheng J, Lu P−R, Xiang D, et al. Retinal image graph−cut segmentation algorithm using multiscale Hessian−enhancement−based nonlocal mean filter. Computational and Mathematical Methods in Medicine 2013;2013.

19.   Metz CE. Some practical issues of experimental design and data analysis in radiological ROC studies. Invest Radiol 1989;24(3):234−45.

20.   Bandos AI, Rockette HE, Song T, Gur D. Area under the

free-response ROC curve (FROC) and a related summary index. Biometrics 2009;65(1):247-56.

21.   Prageeth P, David J, Sukesh Kumar A. Early detection of retinal nerve fiber layer defects using fundus image processing. Recent Advances in Intelligent Computational Systems (RAICS): IEEE, 2011.

22.   Odstrčilík J, Kolář R, Harabiš V, et al. Retinal nerve fiber layer analysis via markov random fields texture modelling. Proc EUSIPCO 2010.

23.   Jan J, Odstrcilik J, Gazarek J, Kolar R. Retinal image analysis aimed at blood vessel tree segmentation and early detection of neural-layer deterioration. Comput Med Imaging Graph 2012;36(6):431-41.

24.   Medeiros FA, Zangwill LM, Bowd C, et al. Evaluation of retinal nerve fiber layer, optic nerve head, and macular thickness measurements for glaucoma detection using optical coherence tomography. Am J Ophthalmol 2005;139(1):44-55.

25.   Wong D, Liu J, Lim J, et al. Automated detection of kinks from blood vessels for optic cup segmentation in retinal images. SPIE Medical Imaging: International Society for Optics and Photonics, 2009.

26.   Radius RL, Anderson DR. The mechanism of disc pallor in

experimental optic atrophy. A fluorescein angiographic study. Arch Ophthalmol 1979;97(3):532−5.

27.   O'Neill EC, Danesh−Meyer HV, Kong GX, et al. Optic disc evaluation in optic neuropathies: the optic disc assessment project. Ophthalmology 2011;118(5):964−70.

28.   Osaguona VB. Differential diagnoses of the pale/white/atrophic disc. Community Eye Health 2016;29(96):71−4.

29.   Hubbard LD, Danis RP, Neider MW, et al. Brightness, contrast, and color balance of digital versus film retinal images in the age−related eye disease study 2. Invest Ophthalmol Vis Sci 2008;49(8):3269−82.

30.   Zenker HJ, Mierdel P, Marre E. Quantitative evaluation of pallor−disc ratio and colour of the optic disc by a photographic method. Graefes Arch Clin Exp Ophthalmol 1983;220(4):184−6.

31.   Sorensen N. The pallor of the optic disc. A quantitative photographic assessment by purple filter. Acta Ophthalmol (Copenh) 1979;57(4):718−24.

32.   Miller JM, Caprioli J. Videographic quantification of optic disc pallor. Invest Ophthalmol Vis Sci 1988;29(2):320−3.

33.   Vilser W, Nagel E, Seifert BU, et al. Quantitative assessment of optic nerve head pallor. Physiol Meas 2008;29(4):451−7.

34.   Nakano E, Hata M, Oishi A, et al. Quantitative comparison of

disc rim color in optic nerve atrophy of compressive optic neuropathy and glaucomatous optic neuropathy. Graefes Arch Clin Exp Ophthalmol 2016;254(8):1609-16.

35. Sagaties Farmer MJ, Schwartz B, Takamoto T. Computerized measurement of the three-dimensional distribution of optic disc pallor. Curr Eye Res 1997;16(11):1096-101.

36. O'Brien C. Optic disc pallor measurement. Eye (Lond) 1991;5 (Pt 6):763-4.

37. Kang S, Kim US. Using ImageJ to evaluate optic disc pallor in traumatic optic neuropathy. Korean J Ophthalmol 2014;28(2):164-9.

38. Schwartz B, Reinstein NM, Lieberman DM. Pallor of the optic disc. Quantitative photographic evaluation. Arch Ophthalmol 1973;89(4):278-86.

39. Hendrickson P, Robert Y, Stockli HP. Principles of photometry of the papilla. Arch Ophthalmol 1984;102(11):1704-7.

40. Aquino A, Gegúndez-Arias ME, Marín D. Detecting the optic disc boundary in digital fundus images using morphological, edge detection, and feature extraction techniques. Medical Imaging, IEEE Transactions on 2010;29(11):1860-9.

41. Cheng J, Liu J, Wong DW, et al. Automatic optic disc segmentation with peripapillary atrophy elimination. Conf Proc IEEE

Eng Med Biol Soc 2011;2011:6224−7.

42.   Oh JE, Yang HK, Kim KG, Hwang JM. Automatic computer−aided diagnosis of retinal nerve fiber layer defects using fundus photographs in optic neuropathy. Invest Ophthalmol Vis Sci 2015;56(5):2872−9.

43.   Jonas JB, Martus P, Budde WM, et al. Small neuroretinal rim and large parapapillary atrophy as predictive factors for progression of glaucomatous optic neuropathy. Ophthalmology 2002;109(8):1561−7.

44.   Paul W. Brazis JCM, José Biller. Localization in clinical neurology 6th ed.: Lippincott Williams & Wilkins, 2012; 157.

45.   Jonas JB, Gusek GC, Naumann G. Optic disc, cup and neuroretinal rim size, configuration and correlations in normal eyes. Investigative ophthalmology & visual science 1988;29(7):1151−8.

46.   Harizman N, Oliveira C, Chiang A, et al. The ISNT rule and differentiation of normal from glaucomatous eyes. Archives of ophthalmology 2006;124(11):1579−83.

47.   Medeiros FA, Zangwill LM, Bowd C, et al. Influence of disease severity and optic disc size on the diagnostic performance of imaging instruments in glaucoma. Investigative ophthalmology & visual science 2006;47(3):1008−15.

48.   Greiner M, Pfeiffer D, Smith R. Principles and practical

application of the receiver-operating characteristic analysis for diagnostic tests. Preventive veterinary medicine 2000;45(1):23-41.

49.   Valenzuela TD, Roe DJ, Cretin S, et al. Estimating effectiveness of cardiac arrest interventions a logistic regression survival model. Circulation 1997;96(10):3308-13.

50.   Pearce J, Ferrier S. Evaluating the predictive performance of habitat models developed using logistic regression. Ecological modelling 2000;133(3):225-45.

51.   Ramm L, Schwab B, Stodtmeister R, et al. Assessment of optic nerve head pallor in primary open-angle glaucoma patients and healthy subjects. Curr Eye Res 2017;42(9):1313-8.

52.   Gargeya R, Leng T. Automated identification of diabetic retinopathy using deep learning. Ophthalmology 2017;124(7):962-9.

53.   Danis RP, Domalpally A, Chew EY, et al. Methods and reproducibility of grading optimized digital color fundus photographs in the Age-Related Eye Disease Study 2 (AREDS2 Report Number 2). Invest Ophthalmol Vis Sci 2013;54(7):4548-54.

54.   Yoshihara N, Yamashita T, Ohno-Matsui K, Sakamoto T. Objective analyses of tessellated fundi and significant correlation between degree of tessellation and choroidal thickness in healthy eyes. PLoS One 2014;9(7):e103586.

55.   Hata M, Miyamoto K, Oishi A, et al. Comparison of optic disc morphology of optic nerve atrophy between compressive optic neuropathy and glaucomatous optic neuropathy. PLoS One 2014;9(11):e112403.

56.   Bourne RR, Stevens GA, White RA, et al. Causes of vision loss worldwide, 1990−2010: a systematic analysis. Lancet Glob Health 2013;1(6):e339−49.

57.   Tham YC, Li X, Wong TY, et al. Global prevalence of glaucoma and projections of glaucoma burden through 2040: a systematic review and meta−analysis. Ophthalmology 2014;121(11):2081−90.

58.   Quigley HA, Broman AT. The number of people with glaucoma worldwide in 2010 and 2020. Br J Ophthalmol 2006;90(3):262−7.

59.   Iwase A, Suzuki Y, Araie M, et al. The prevalence of primary open−angle glaucoma in Japanese: the Tajimi Study. Ophthalmology 2004;111(9):1641−8.

60.   Kim CS, Seong GJ, Lee NH, et al. Prevalence of primary open−angle glaucoma in central South Korea the Namil study. Ophthalmology 2011;118(6):1024−30.

61.   Health Quality O. Routine eye examinations for persons 20−64 years of age: an evidence−based analysis. Ont Health Technol

Assess Ser 2006;6(15):1-81.

62.   McKean-Cowdin R, Wang Y, Wu J, et al. Impact of visual field loss on health-related quality of life in glaucoma: the Los Angeles Latino Eye Study. Ophthalmology 2008;115(6):941-8 e1.

63.   Burr JM, Mowatt G, Hernandez R, et al. The clinical effectiveness and cost-effectiveness of screening for open angle glaucoma: a systematic review and economic evaluation. Health Technol Assess 2007;11(41):iii-iv, ix-x, 1-190.

64.   Jonas JB, Budde WM, Panda-Jonas S. Ophthalmoscopic evaluation of the optic nerve head. Surv Ophthalmol 1999;43(4):293-320.

65.   Jonas JB, Schiro D, Naumann GO. The retinal nerve fiber layer in normal and glaucoma eyes. Ophthalmologe 1993;90(6):603-12.

66.   Jonas JB, Schiro D. Localized retinal nerve fiber layer defects in nonglaucomatous optic nerve atrophy. Graefes Arch Clin Exp Ophthalmol 1994;232(12):759-60.

67.   Iwata K, Nanba K, Abe H. Typical slit-like retinal nerve fiber layer defect and corresponding scotoma (author's transl). Nippon Ganka Gakkai Zasshi 1981;85(10):1791-803.

68.   Airaksinen PJ, Mustonen E, Alanko HI. Optic disc haemorrhages precede retinal nerve fibre layer defects in ocular

hypertension. Acta Ophthalmol (Copenh) 1981;59(5):627-41.

69.   Sommer A, Katz J, Quigley HA, et al. Clinically detectable nerve fiber atrophy precedes the onset of glaucomatous field loss. Arch Ophthalmol 1991;109(1):77-83.

70.   Quigley HA, Reacher M, Katz J, et al. Quantitative grading of nerve fiber layer photographs. Ophthalmology 1993;100(12):1800-7.

71.   Vermeer KA, Reus NJ, Vos FM, et al. Automated detection of wedge-shaped defects in polarimetric images of the retinal nerve fibre layer. Eye (Lond) 2006;20(7):776-84.

72.   Horn FK, Nguyen NX, Mardin CY, Junemann AG. Combined use of frequency doubling perimetry and polarimetric measurements of retinal nerve fiber layer in glaucoma detection. Am J Ophthalmol 2003;135(2):160-8.

73.   Niessen AG, Van Den Berg TJ, Langerhorst CT, Greve EL. Retinal nerve fiber layer assessment by scanning laser polarimetry and standardized photography. Am J Ophthalmol 1996;121(5):484-93.

74.   Niessen AG, van den Berg TJ, Langerhorst CT, Bossuyt PM. Grading of retinal nerve fiber layer with a photographic reference set. Am J Ophthalmol 1995;120(5):577-86.

75.   Niessen AG, van den Berg TJ. Evaluation of a reference set

based grading system for retinal nerve fiber layer photographs in 1941 eyes. Acta Ophthalmol Scand 1998;76(3):278-82.

76.　　Niessen AG, Langerhorst CT, Geijssen HC, Greve EL. Design of low cost glaucoma screening. Doc Ophthalmol 1997;93(4):293-315.

77.　　Komulainen R, Tuulonen A, Airaksinen PJ. The follow-up of patients screened for glaucoma with non-mydriatic fundus photography. Int Ophthalmol 1992;16(6):465-9.

78.　　Tuulonen A, Alanko H, Hyytinen P, et al. Digital imaging and microtexture analysis of the nerve fiber layer. J Glaucoma 2000;9(1):5-9.

79.　　Lee SY, Kim KK, Seo JM, et al. Automated quantification of retinal nerve fiber layer atrophy in fundus photograph. Conf Proc IEEE Eng Med Biol Soc 2004;2:1241-3.

80.　　Kolar R, Tornow RP, Laemmer R, et al. Analysis of visual appearance of retinal nerve fibers in high resolution fundus images: a study on normal subjects. Comput Math Methods Med 2013;2013:134543.

81.　　Canny J. A computational approach to edge detection. IEEE Trans Pattern Anal Mach Intell 1986;8(6):679-98.

82.　　Wang F, Quigley HA, Tielsch JM. Screening for glaucoma in a medical clinic with photographs of the nerve fiber layer. Arch

Ophthalmol 1994;112(6):796-800.

83.　　Sugiyama K, Uchida H, Tomita G, et al. Localized wedge-shaped defects of retinal nerve fiber layer and disc hemorrhage in glaucoma. Ophthalmology 1999;106(9):1762-7.

요약(국문초록)

시신경병증의 진단에서 가장 기초적인 단계는 안저사진에서 시신경의 구조적 이상을 확인하는 것이다. 그러나 다양한 질환에서 시신경의 형태가 유사하게 보일 수 있으며, 안저사진에서 시신경의 모양만으로 다양한 시신경병증을 감별하는 것은 쉽지 않다. 최근 빛간섭단층촬영을 포함한 고해상도의 측정 장비가 널리 이용되지만, 아직까지 비용효과와 편리함을 이유로 망막질환과 시신경질환의 진단을 위해 대부분의 건강검진기관이나 일차의료기관에서는 디지털 안저사진을 촬영한다. 디지털 안저사진의 판독은 검사자의 주관적인 판단에 의존하므로 검사자에 의한 오진 가능성이 있다. 따라서, 이 연구에서는 안저사진 판독의 정확도와 효율성을 높이기 위해 자동화된 컴퓨터보조진단 시스템을 개발하였다. 개발된 시스템은 정상안저와 비교하여 망막신경섬유층결손과 시신경창백을 각각 94%, 96%의 정확도로 검출하였고, 단일 건강검진기관에서 시행한 대규모 선별검사에서 90%의 정확도로 시신경질환을 진단하였다.

....